Magnetothermal properties of $Ho_{1-x}Dy_xAl_2$ (x = 0, 0.05, 0.10, 0.15, 0.25 and 0.50) compounds

P. O. Ribeiro[1,2], B. P. Alho[2,3] R. S. De Oliveira[3], E. P. Nóbrega[3], V. S. R. de Sousa[3],

P. J. von Ranke[3], Anis Biswas[2], Mahmud Khan[4], Y. Mudryk[2], V.K. Pecharsky[2,5]

[1] Instituto de Aplicação Fernando Rodrigues da Silveira, Universidade do Estado do Rio de Janeiro – UERJ, Rua Santa Alexandrina 288, 20261-232 RJ, Brazil.

[2] The Ames Laboratory, U.S. Department of Energy, Iowa State University, Ames, IA, 50011-3020, USA.

[3] Instituto de Física, Universidade do Estado do Rio de Janeiro - UERJ, Rua São Francisco Xavier, 524, 20550-013, RJ, Brazil.

[4] Department of Physics, Miami University, Oxford, OH, 45056, USA.

[5] Department of Materials Science and Engineering, Iowa State University, Ames, IA, 50011-2300, USA.

Corresponding Author: P. O. Ribeiro

Universidade do Estado do Rio de Janeiro, CAp - DCN

Rua Santa Alexandrina, 288.

Rio comprido - Rio de Janeiro – 20261-232, Brazil.

E-mail: paula.ribeiro@gmail.com

Abstract

Magnetic and magnetocaloric properties of $\mathrm{Ho}_{1-x}\mathrm{Dy}_x\mathrm{Al}_2$ compounds with $x = 0, 0.05, 0.10$, 0.15,0.25 and 0.50, modelled using a Hamiltonian that includes the exchange interactions between Ho-Dy, Ho-Ho and Dy-Dy ions in addition to the crystalline electric field and the Zeeman effects, have been compared with those determined experimentally. In order to reproduce experimentally observed global ferromagnetic ordering temperatures and spin reorientation transition temperatures as x_{Dy} varies, the exchange interactions between Ho-Dy and Ho-Ho were set as free parameters and adjusted to match the experimental results. We demonstrate that heat capacity of polycrystalline materials in non-zero magnetic fields can be satisfactory reproduced by using the average of multiple magnetic field directions with respect to the crystallographic coordinate system, while reasonably good agreement between experimentally determined and theoretically predicted magnetocaloric effects can be achieved considering an average of only three field directions.

Keywords: mean-field modeling; magnetocaloric effect; rare earths; crystalline electrical field; polycrystalline sample.

1. Introduction

Climate change represents a major global challenge of our times. Overcoming this challenge must include addressing rising energy consumption and mitigating the growing use of chemicals with high global-warming potential, both of which are foreseeable due to the accelerating demand for cooling devices around the world. For example, Brazil averages 0.4 air conditioning units per household today, that is, 2.5-5 times less when compared to 1-2 units per household in developed countries, such as the United States [1]. The acceleration of the demand for cooling is further compounded by the projections showing that African, South Asian, Central and South American countries, including Brazil, are projected to experience extreme temperatures more frequently over the next few decades due to the changing climate [2]. In order to satisfy the cooling needs and to sustain the quality of life, rapid progress in advanced energy-saving technologies that can replace the omnipresent vapor compression refrigeration is, therefore, of great importance.

Among the most promising replacement technologies is magnetocaloric heat pumping – a solid-state approach based on the magnetocaloric effect (MCE) [3]. In a magnetocaloric refrigerator or air conditioner, a volatile liquid refrigerant is replaced with a solid magnetocaloric refrigerant that reversibly changes its temperature in response to an oscillating magnetic field. Magnetocaloric solids have zero global warming potential and cannot escape into the environment. Laboratory demonstrations of magnetocaloric heat pumps show thermodynamic efficiencies nearly on par with those of vapor compression systems [4]. Further improvements, however, require magnetocaloric materials that exhibit stronger MCEs in lower magnetic fields and with minimum energy losses [5].

In addition to tremendous technological importance, MCE is of significance to basic science. Expressed as one or both thermodynamic parameters, that are, magnetic field induced isothermal entropy change, ΔS_T, and adiabatic temperature change, ΔT_{ad}, magnetocaloric effect is intimately related to other fundamental physical properties of magnetic materials. Among those are individual magnetic moments, exchange interactions, global and local magnetic ordering and spin reorientation phase transformations, bulk magnetization, heat capacity, electronic and lattice entropies, and their dependencies on chemistry and structure, as well as magnetic field and temperature [6–8]. Amid many potential candidates suitable to both understand and tailor these properties is an extended series of pseudobinary $\mathrm{R}_{1-x}\mathrm{R}'_x\mathrm{Al}_2$ compounds adopting cubic Laves

phase structure, where properties can change dramatically with concentration (x) and the nature of the rare-earth constituents (R and R′) [9–12].

In 2011 Khan and coworkers [13] experimentally examined the $Ho_{1-x}Dy_xAl_2$ family, where $x = 0, 0.05, 0.10, 0.15, 0.25,$ and 0.50. They confirmed a spontaneous spin reorientation (SSR) transition between $\langle 110 \rangle$ and $\langle 100 \rangle$ easy magnetization directions at 20 K in $HoAl_2$ reported earlier [14] and showed that introduction of Dy into the Ho sublattice affects the SSR. The thermodynamic nature of the spin reorientation gradually changes from first- to second-order as the Dy concentration increases. Later, de Sousa *et al.* [15] associated the SSR in $HoAl_2$ with a spontaneous change in the free energy, and demonstrated that at temperatures lower than 20 K the $\langle 110 \rangle$ easy magnetization direction is the state with lowest energy, but at $T > 20$ K, $\langle 100 \rangle$ becomes the preferred direction of the localized magnetic moments of Ho. These results are reminiscent of the behavior observed in $HoCo_2$ [16], where the $\langle 110 \rangle \rightarrow \langle 100 \rangle$ spin reorientation is accompanied by the orthorhombic → tetragonal crystallographic distortion. The finite temperature theoretical modeling of the magnetothermal behavior in mixed rare-earth alloys with complex crystalline electric field contributions will lead to better understanding of the effect that this and similar order-order transformations have on the magnetocaloric effect. In particular, achieving capability of quantitative predictions of MCE in mixed rare earth $R_{1-x}R'_xAl_2$ compounds, which are important materials systems for cryogenic applications [17,18], remains a challenging but highly desired outcome for theoretical modeling. Thus, in this work we revisit available experimental data of the $Ho_{1-x}Dy_xAl_2$ series and rationalize them using the mean field approach. We compare theoretically predicted heat capacity, C_p, ΔS_T, and ΔT_{ad} with the experimental data published in [13] as well as with additional heat capacity measurements performed in this study for $x = 0.10$ and $x = 0.50$ in 1 and 2 T applied magnetic fields.

2. Theory

To describe the magnetic and thermal properties of cubic C15 Laves phase pseudobinary $Ho_{1-x}Dy_xAl_2$, model Hamiltonians in the mean field approximation [10,19,20] include contributions accounting for exchange interactions of the individual magnetic moments, the applied magnetic field (Zeeman effect), and the crystalline electrical field (CEF). Thus, the coupled Hamiltonians are given by

$$\mathcal{H}^{\mathrm{Ho}} = -g^{\mathrm{Ho}}\mu_B\left[\lambda_{HoHo}\vec{M}^{\mathrm{Ho}} + \lambda_{HoDy}\vec{M}^{\mathrm{Dy}} + \mu_0\vec{H}\right]\cdot\vec{J}^{\mathrm{Ho}} + \mathcal{H}^{\mathrm{Ho}}_{\mathrm{CEF}}, \qquad (1)$$

$$\mathcal{H}^{\mathrm{Dy}} = -g^{\mathrm{Dy}}\mu_B\left[\lambda_{DyDy}\vec{M}^{\mathrm{Dy}} + \lambda_{HoDy}\vec{M}^{\mathrm{Ho}} + \mu_0\vec{H}\right]\cdot\vec{J}^{\mathrm{Dy}} + \mathcal{H}_{\mathrm{CEF}}^{\mathrm{Dy}}. \quad (2)$$

The first two terms in equations (1) and (2) take into account the intra-sublattice exchange interactions (λ_{HoHo} and λ_{DyDy}) between identical rare earth ions, as well as inter-sublattice exchange (λ_{HoDy}) between Ho and Dy. Here, μ_B is the Bohr magneton, $g^{\mathrm{Ho}} = 5/4, g^{\mathrm{Dy}} = 4/3$ are the Landè factors, $\vec{M}^{\mathrm{Ho}}$ and $\vec{M}^{\mathrm{Dy}}$ are, respectively, the magnetization vectors for Ho and Dy sublattices, and $J^{\mathrm{Ho}} = 8, J^{\mathrm{Dy}} = 15/2$ are the total angular momenta. The third terms account for Zeeman effect due to the applied magnetic field ($\mu_0\vec{H}$, where μ_0 is permeability of vacuum and $\vec{H}$ is the auxiliary field), and the last terms describe CEF. Because the $\mathrm{Ho}_{1-x}\mathrm{Dy}_x\mathrm{Al}_2$ compounds have cubic structure [13] and the crystallographic distortions are minor, the CEF Hamiltonian, for each rare earth sublattice, is written in the Lea-Leask-Wolf notation [21]:

$$\mathcal{H}_{CEF} = W\left[X\left(\frac{O_4^0 + 5O_4^4}{F_4}\right) + (1 - |X|)\left(\frac{O_6^0 - 21O_6^4}{F_6}\right)\right], \quad (3)$$

where W and X are the CEF parameters for each rare earth sublattice (Ho and Dy), and F_4 and F_6 are common constants. Following the literature [21–23], the W, X, F_4 and F_6 are set as follows: $W^{\mathrm{HoAl_2}} = 0.015$ meV, $W^{\mathrm{DyAl_2}} = -0.011$ meV, $X^{\mathrm{HoAl_2}} = -0.34$, $X^{\mathrm{DyAl_2}} = 0.30$, $F_4^{\mathrm{HoAl_2}} = F_4^{\mathrm{DyAl_2}} = 60$ and $F_6^{\mathrm{HoAl_2}} = F_6^{\mathrm{DyAl_2}} = 13860$. O_4^0, O_4^4, O_6^0 and O_6^4 are the fourth and sixth order Stevens operators, respectively [24,25].

Magnetization and magnetic entropies $S_{mag}^{\mathrm{R}}\left(T, \mu_0\vec{H}\right)$ for each magnetic sublattice are obtained from the eigenvectors and eigenvalues calculated from the Hamiltonians (1), (2) and (3) [12,23,26]. Further, the lattice vibrational entropies $S_{lat}^{\mathrm{R}}(T)$ are given in the Debye approximation and the electronic $S_{el}^{\mathrm{R}}(T)$ are treated as linear functions of temperature [23,27]. The total entropies $S_{total}^{\mathrm{R}}\left(T, \mu_0\vec{H}\right)$ for each of the rare-earth sublattices (R = Ho and Dy) are sums of these three contributions. For the intermediate compositions within the series, $\mathrm{Ho}_{1-x}\mathrm{Dy}_x\mathrm{Al}_2$, effects of disorder are taken into account as [28]:

$$S_{total}^{x}\left(T, \mu_0\vec{H}\right) = (1-x)S_{total}^{\mathrm{Ho}} + (x)S_{total}^{\mathrm{Dy}}. \quad (4)$$

With the determined total entropy $S_{total}^{x}\left(T, \mu_0\vec{H}\right)$, the heat capacities and the magnetocaloric effects are calculated:

$$C_p^x\left(T, \mu_0\vec{H}\right) = T\left(\frac{\partial S_{total}^x}{\partial T}\right), \quad (5)$$

$$\Delta S_T^x\,(T, \mu_0 H) = S_{total}^x(T, \mu_0 H \neq 0) - S_{total}^x(T, \mu_0 H = 0), \quad (6)$$

$$\Delta T_{ad}^{x}\,(T,\mu_0 H) = T(S^x,\mu_0 H \neq 0) - T(S^x,\mu_0 H = 0). \qquad (7)$$

3. Experimental

Polycrystalline samples with x = 0.1 and 0.5 used for the heat capacity measurements were taken from the same alloys that were prepared and characterized in reference [13]. The heat capacity was measured using the relaxation technique in a Quantum Design Physical Property Measurement System (PPMS). The measurements were performed in magnetic fields $\mu_0 H$ = 0, 1, and 2 T from 3 to 70 K. The zero field data, as expected, match the data reported previously [13]. For other compounds (x = 0, 0.05, 0.15 and 0.25) heat capacity data measured with and without magnetic field were taken from reference [13].

4. Results and discussion

In order to model the magnetic and magnetocaloric properties in the $Ho_{1-x}Dy_xAl_2$ series, we used the Debye temperature, $\Theta_D = 300$ K, and the Sommerfeld coefficient, $\gamma = 5.4$ mJ/(mol K^2), as reported earlier [23]. The exchange parameters, λ_{HoHo}, λ_{DyDy}, and λ_{HoDy} were adjusted for each investigated Dy concentration, x_{Dy}, to reproduce the heat capacity data of Ref. [13] without the applied magnetic field. As mentioned earlier, the easy magnetization direction in the $HoAl_2$ sublattice changes from $\langle 110 \rangle$ at high temperature to $\langle 100 \rangle$ at low temperature, and in $DyAl_2$ the easy magnetization direction remains $\langle 100 \rangle$ in the temperature range of interest [11,29,30]. Hence, assigning $\lambda_{DyDy} = x_{\mathrm{Dy}} \cdot (0.258\ \mathrm{meV})$, where 0.258 meV is the exchange parameter of pure $DyAl_2$ [12,23] reflects the linear increase of T_C with x_{Dy}. The values of λ_{HoHo} and λ_{HoDy} were adjusted for each Dy concentration when $x_{\mathrm{Dy}} < 1$ in order to better reproduce the experimental values of T_C and T_{SR} [13,22]. In the absence of external magnetic field, the experimentally measured (symbols) [13] and modelled heat capacities (solid lines) for the 6 investigated compositions are in a good agreement, as illustrated in Fig. 1. In addition to accurately reproducing the temperatures of the global ferromagnetic ordering, T_C, and the spin reorientation (SR), T_{SR}, the model also correctly estimates the order of the $\langle 110 \rangle \rightarrow \langle 100 \rangle$ SR phase transitions, which changes from the first order for $x = 0$ (Fig. 1a) and $x = 0.05$ (Fig. 1b), to the second order for all other members of the series (Fig. 1c-f), in full agreement with the experiment [13]. Another experimental behavior reproduced in the simulated heat capacity (solid lines in Fig.1) is the

reduction of T_{SR} and increase of T_C with increasing x_{Dy}. The three exchange parameters are depicted in Fig. 2 as functions of x_{Dy}.

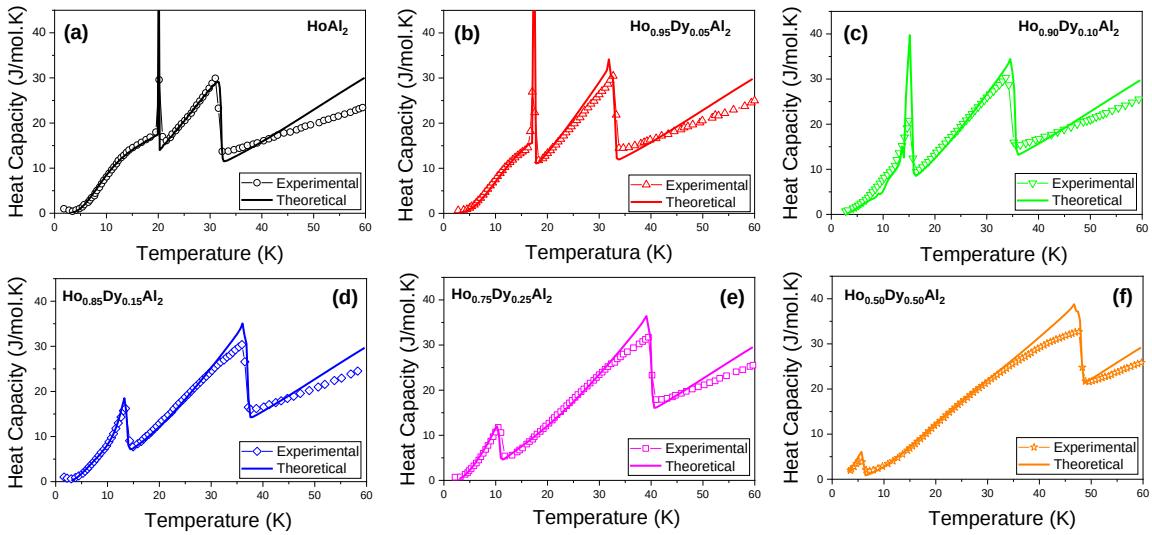

Figure 1 Temperature dependencies of the heat capacities of (a) $HoAl_2$, (b) $Ho_{0.95}Dy_{0.05}Al_2$, (c) $Ho_{0.90}Dy_{0.10}Al_2$, (d) $Ho_{0.85}Dy_{0.15}Al_2$, (e) $Ho_{0.75}Dy_{0.25}Al_2$ and (f) $Ho_{0.50}Dy_{0.50}Al_2$ measured in zero magnetic field. The symbols are the data of experimental measurements [13] and the solid lines are computed using the formalism described in Section 3.

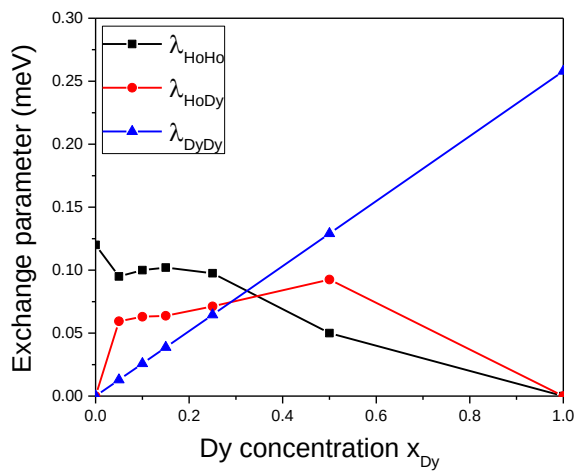

Figure 2 Exchange parameters (λ_{HoHo}, λ_{DyDy} and λ_{HoDy}) shown as functions of Dy concentration x_{Dy}.

Figure 3 compares modeled $C_p(T)$ (gray solid lines) with experimental data (symbols) from Ref [13] (Fig. 3a, Fig. 3b, Fig. 3d and Fig. 3e) and new measurements (Fig. 3c and Fig. 3f), with $\mu_0 H = 1$ T. The model described in Section 3 assumes anisotropic, single-domain single crystals with the

magnetic field applied along selected crystallographic directions. The experimental measurements, on the other hand, were performed using isotropic polycrystalline materials. In the first approximation, the heat capacities of isotropic polycrystalline cubic materials, $C_p^{iso}(T)$, are often modeled using simple averages: $C_p^{iso}(T) = \left[C_p^{\vec{H}||<100>}(T) + C_p^{\vec{H}||<110>}(T) + C_p^{\vec{H}||<110>}(T)\right]/3$. Although simple averages can be effective in reproducing experimental data for some compounds [20,31], this is clearly not the case for $Ho_{1-x}Dy_xAl_2$, and the averaging should include additional field directions in reference to the crystallographic coordinate system. This has been accomplished by averaging the results with the magnetic field parallel to a much larger number of crystallographic directions. The orientational relationships have been described by introducing polar (θ_i) and azimuthal (ϕ_j) angles defined as the angles the magnetic field vector forms with the Z axis (θ_i) and with the X axis in the XY plane (ϕ_j), as illustrated in Fig. 4.

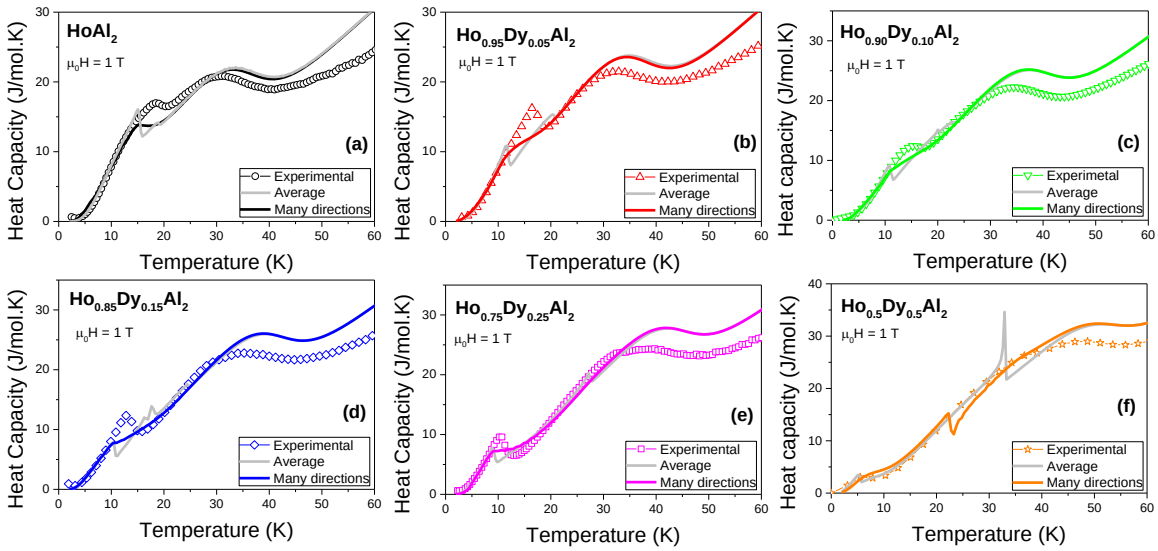

Figure 3 Temperature dependencies of the heat capacity in $\mu_0 H = 1$ T applied magnetic field for (a) $HoAl_2$, (b) $Ho_{0.95}Dy_{0.05}Al_2$, (c) $Ho_{0.90}Dy_{0.10}Al_2$, (d) $Ho_{0.85}Dy_{0.15}Al_2$, (e) $Ho_{0.75}Dy_{0.25}Al_2$, and (f) $Ho_{0.50}Dy_{0.50}Al_2$. Symbols represent experimental measurements and lines represent theoretical simulations. The gray lines represent simple averages $C_p^{iso}(T) = \left[C_p^{\vec{H}||<100>}(T) + C_p^{\vec{H}||<110>}(T) + C_p^{\vec{H}||<110>}(T)\right]/3$, and colored lines depict averages computed using Eq. 8.

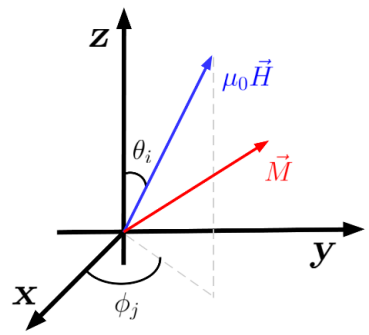

Figure 4 Illustration of the correlation of cartesian (x, y, z) and spherical coordinates (r, θ, ϕ), for the applied magnetic field ($\mu_0\vec{H}$). In spherical coordinates, $\mu_0\vec{H}$ is described as $(r, \theta, \phi) = (\mu_0 H, \theta_i, \phi_j)$.

For each θ_i and ϕ_j, the corresponding values of $C_p^{\vec{H}||(\theta_i,\phi_j)}(T)$ were calculated in the first octant $(0 \leq \theta_i,\ \phi_j \leq 90^0)$ and averaged as follows:

$$\frac{1}{n_i \cdot n_j} \sum_{i=0}^{n_i} \sum_{j=0}^{n_j} C_p^{\vec{H}||(\theta_i,\phi_j)}(T)\,, \tag{8}$$

where $n_i = 20$ and $n_j = 20$ are the number of grid points in polar and azimuthal angle coordinates, respectively. The results obtained using Eq. 8 are shown in Figure 3 as colored solid lines, demonstrating significant improvement over the model of simple averages except when $x = 0.50$. Modelling heat capacity with the magnetic field applied along more orientations than the three main crystallographic directions, smooths out the sharp anomalies that appear in the theoretical results due to spin reorientation transitions. The sharp heat capacity anomalies are most pronounced with the magnetic field parallel to [111] and are non-existent when the field is parallel to [100], but experimentally the SR processes in a non-zero magnetic field are seen as changes of slope around T_{SR}, likely due to the polycrystalline nature of the samples.

For $Ho_{0.5}Dy_{0.5}Al_2$ (Fig. 3f) a rather sharp anomaly remains in the theoretical results around T = 22.3 K even after the averaging using Eq. 8 due to spin reorientation processes occurring at the same temperature in both sublattices. This is illustrated in Figure 5, which shows the temperature dependencies of the magnetization components, M_x, M_y and M_z of both magnetic sublattices with $\mu_0 H = 1$ T applied in one of the many examined directions, namely with $\theta_i = 18.4°$ and $\phi_j = 67.3°$. At low temperatures, due to the intersublattice exchange and the interactions with the

magnetic field, both Ho and Dy sublattices are not aligned with the easy magnetization directions, ⟨110⟩ and ⟨100⟩, respectively, of their corresponding binary compounds. When T < 24 K the energetically favorable magnetization vectors ($\vec{M}$) for both rare earth sublattices are close to the XY plane, but as the thermal excitations increase (T > 24 K) they sharply rotate and align closely with the direction of the applied magnetic field. Similar abrupt rotations are also observed with magnetic field applied in a few other directions used to calculate the multipoint average, resulting in a sharp transition seen in the orange curve of Fig. 3f.

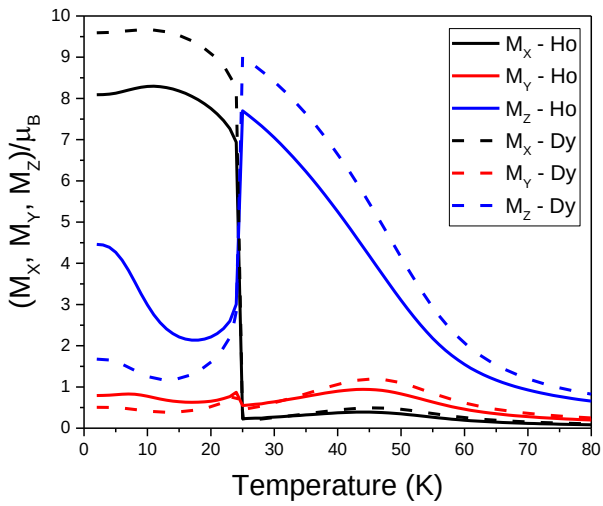

Figure 5 Magnetization components M_X, M_Y and M_Z of each rare-earth sublattice *vs.* temperature with $\mu_0 H = 1$ T magnetic field applied along direction with $\theta_i = 18.4$ ° and $\phi_j = 67.3°$. Solid lines are for Ho and dashed lines are for Dy sublattices.

The same systematic analyses were performed for the isothermal entropy change (Figure 6) and adiabatic temperature change (Figure 7). Although including many magnetic field orientation directions into the averaging (equation (8)) makes the model more accurate for the heat capacity, for ΔS_T and ΔT_{ad} the differences in results obtained by two different averaging models are negligible. The simple averaging (along the main three crystallographic directions only) reproduces the experimentally observed magnetocaloric effects around T_{SR} and T_C reasonably well. This may be associated with the fact that in our model ΔS_T and ΔT_{ad} are calculated directly from the computed total entropy, whereas C_p is obtained from the thermodynamic relation $C_p = T\frac{\partial S}{\partial T}$. Since C_p calculations involve differentiation, minor discontinuities in the total entropy

become clearly visible as sharp heat capacity anomalies, but they are masked in the entropy curves, as well as in their isothermal and isentropic differences, that are, respectively, ΔS_T and ΔT_{ad}.

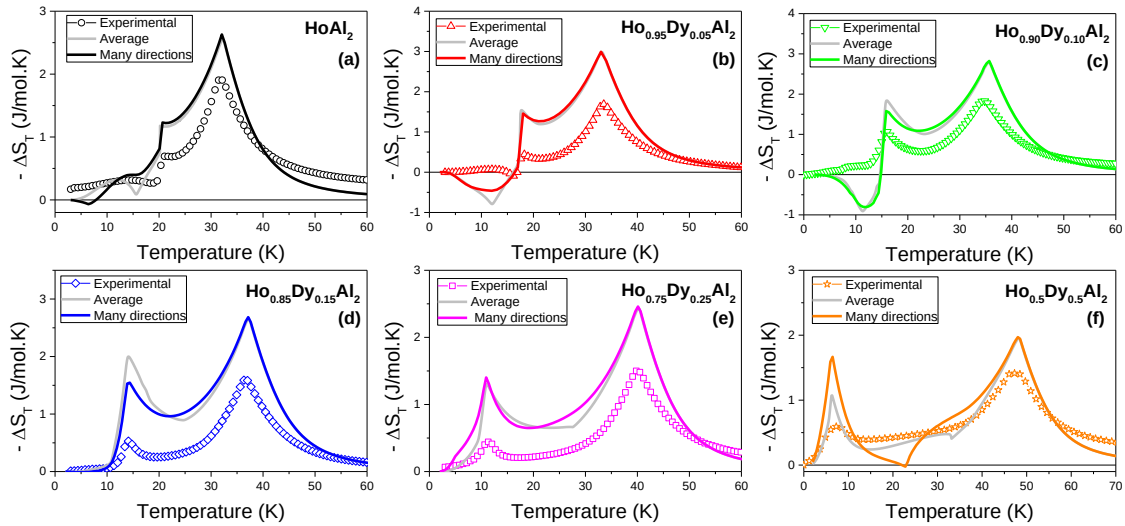

Figure 6 Temperature dependencies of isothermal entropy change upon magnetic field change of $\mu_0 \Delta H = 1$ T for (a) $HoAl_2$, (b) $Ho_{0.95}Dy_{0.05}Al_2$, (c) $Ho_{0.90}Dy_{0.10}Al_2$, (d) $Ho_{0.85}Dy_{0.15}Al_2$, (e) $Ho_{0.75}Dy_{0.25}Al_2$ and (f) $Ho_{0.50}Dy_{0.50}Al_2$. The symbols are the experimental measurements and the solid lines are the theoretical simulations. The gray lines represent the simple average with the magnetic field along three main crystallographic directions, and the colored lines represent averaging according to Eq. (8).

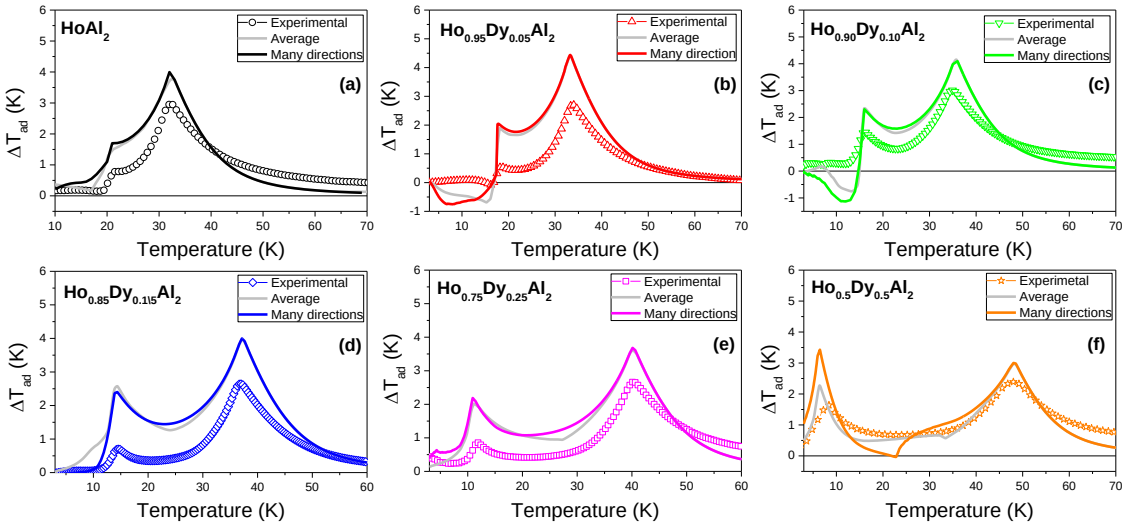

Figure 7 Temperature dependencies of adiabatic temperature change upon magnetic field change of $\mu_0 \Delta H = 1$ T for (a) $HoAl_2$, (b) $Ho_{0.95}Dy_{0.05}Al_2$, (c) $Ho_{0.90}Dy_{0.10}Al_2$, (d) $Ho_{0.85}Dy_{0.15}Al_2$, (e) $Ho_{0.75}Dy_{0.25}Al_2$ and (f) $Ho_{0.50}Dy_{0.50}Al_2$. The symbols are the experimental measurements and the solid lines are the theoretical simulations. The gray lines represent the simple average with the magnetic field along three main crystallographic directions, and the colored lines represent averaging according to Eq. (8).

Figures 8 and 9 show the experimental and theoretical results for magnetocaloric effect with applied magnetic field change of $\mu_0\Delta H = 2$ T for x_{Dy} = 0.1 and 0.5. As observed previously [13], for $\mu_0\Delta H$ = 2 T, higher x leads to lower peak values in $-\Delta S_T(T)$ and $\Delta T_{ad}(T)$ at T_C. For example, from $x = 0.10$ to $x = 0.50$ for $\mu_0\Delta H = 2$ T, experimentally determined $-\Delta S_T(T)$ peaks at T_C change from ~ 3 J/mol.K (Fig. 8a) to ~ 2.4 J/mol.K (Fig. 8b) and $\Delta T_{ad}(T)$ peaks from ~ 5 K (Fig. 9a) to ~ 4 K (Fig. 9b). This is expected because as T_C increases with x_{Dy} (from 31.6 K for $HoAl_2$ to 63 K for $DyAl_2$), the derivative of the magnetization with respect to temperature becomes smaller and the lattice heat capacity becomes larger, resulting in the gradual reduction of both MCE parameters.

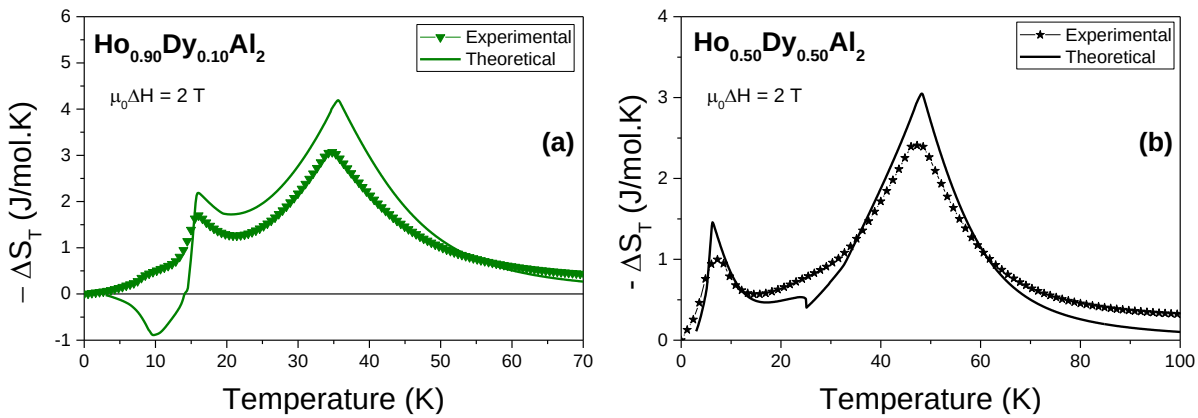

Figure 8 Isothermal entropy change vs. temperature for (a) $Ho_{0.90}Dy_{0.10}Al_2$ and (b) $Ho_{0.50}Dy_{0.50}Al_2$, upon applied magnetic field change of $\mu_0\Delta H = 2$ T. The symbols are the new experimental measurements and the solid lines the theoretical simulations calculated with an average of the main cubic directions: $\langle 100\rangle, \langle 110\rangle$ and $\langle 111\rangle$.

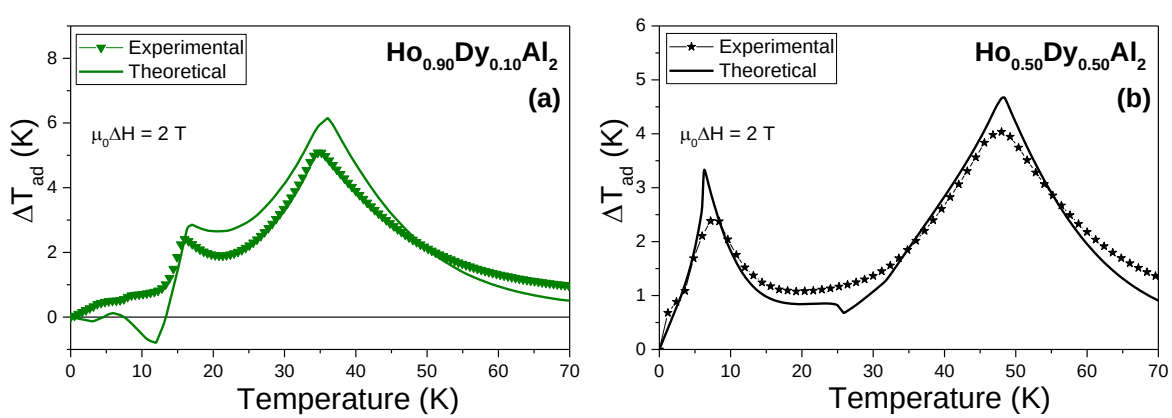

Figure 9 Adiabatic temperature change vs. temperature for (a) $Ho_{0.90}Dy_{0.10}Al_2$ and (b) $Ho_{0.50}Dy_{0.50}Al_2$, upon applied magnetic field change of $\mu_0 \Delta H = 2$ T. The symbols are the new experimental measurements and the solid lines the theoretical simulations calculated with an average of the main cubic directions: $\langle 100 \rangle, \langle 110 \rangle$ and $\langle 111 \rangle$.

5. Conclusions

Our systematic investigation of heat capacity of six compounds in the series $Ho_{1-x}Dy_xAl_2$ with x = 0, 0.05, 0.10, 0.15, 0.25 and 0.50 shows that mean-field modeling reproduces the changes in T_C and T_{SR}, as well as the changes in the thermodynamic nature of the spin reorientation phase transitions process observed experimentally as the Dy concentration increase. The agreement between experimental heat capacity data measured using polycrystalline materials and calculations performed assuming single-domain anisotropic crystals significantly improves by considering an average of the multiple applied field directions rather than commonly employed averaging of results obtain with field applied parallel to three main crystallographic directions in cubic materials. This method can be applied to other compounds in order to improve the agreement between heat capacity derived from theory and experiments. However, we found that this approach was not necessary for modeling the temperature dependencies of magnetocaloric effect, that can be reproduce and satisfactory predicted considering a simple average of the results obtained with the magnetic field applied along 3 main cubic directions, $\langle 100 \rangle$, $\langle 110 \rangle$ and $\langle 111 \rangle$.

Acknowledgments

The Ames Laboratory is operated for the U. S. Department of Energy (DOE) by Iowa State University of Science and Technology under contract No. DE-AC02-07CH11358. This work was supported by the Office of Science of the U.S. DOE, Division of Materials Sciences and Engineering, Office of Basic Energy Sciences. POR and BPA acknowledges the financial support of Coordenação de Aperfeiçoamento de Pessoal de Nível Superior – Brasil (CAPES) – Finance Code 001, CNPq – Conselho Nacional de Desenvolvimento Científico e Tecnológico – Brazil and FAPERJ - Fundação de Amparo à Pesquisa do Estado do Rio de Janeiro.

References

[1] Ministério de Minas e Energia, Uso de Ar Condicionado no Setor Residencial Brasileiro: Perspectivas e contribuições para o avanço em eficiência energética, Nota Técnica EPE 030/2018 - . (2018) 43. http://epe.gov.br/sites-pt/publicacoes-dados-abertos/publicacoes/PublicacoesArquivos/publicacao-341/NT EPE 030_2018_18Dez2018.pdf.

[2] Q. Schiermeier, Clear signs of global warming will hit poorer countries first, Nature. 556 (2018) 415–416. https://doi.org/10.1038/d41586-018-04854-2.

[3] G. V. Brown, Magnetic heat pumping near room temperature, J. Appl. Phys. 47 (1976) 3673–3680. https://doi.org/10.1063/1.323176.

[4] L. Griffith, A. Czernuszewicz, J. Slaughter, V. Pecharsky, CaloriSMART: Small-scale test-stand for rapid evaluation of active magnetic regenerator performance, Energy Convers. Manag. 199 (2019) 111948. https://doi.org/10.1016/j.enconman.2019.111948.

[5] V.K. Pecharsky, J. Cui, D.D. Johnson, (Magneto)caloric refrigeration: is there light at the end of the tunnel?, Philos. Trans. R. Soc. A Math. Phys. Eng. Sci. 374 (2016) 20150305. https://doi.org/10.1098/rsta.2015.0305.

[6] K.A. Gschneidner, V.K. Pecharsky, Magnetic refrigeration materials (invited), J. Appl. Phys. 85 (1999) 5365–5368. https://doi.org/10.1063/1.369979.

[7] V. Franco, J.S. Blázquez, J.J. Ipus, J.Y. Law, L.M. Moreno-Ramírez, A. Conde, Magnetocaloric effect: From materials research to refrigeration devices, Prog. Mater. Sci. 93 (2018) 112–232. https://doi.org/10.1016/j.pmatsci.2017.10.005.

[8] M.S. Reis, Magnetocaloric and barocaloric effects of metal complexes for solid state cooling: Review, trends and perspectives, Coord. Chem. Rev. 417 (2020) 213357. https://doi.org/10.1016/j.ccr.2020.213357.

[9] H. Adachi, H. Ino, A ferromagnet having no net magnetic moment, Nature. 401 (1999) 148–150. https://doi.org/10.1038/43634.

[10] N.A. de Oliveira, P.J. von Ranke, Magnetocaloric effect in the Laves phase pseudobinaries $(Dy_{1-c}R_c)Al_2$ (R = Er and Ho), J. Magn. Magn. Mater. 320 (2008) 386–392. https://doi.org/10.1016/j.jmmm.2007.06.014.

[11] M. Khan, A.K. Pathak, Y. Mudryk, K.A. Gschneidner, Jr., V.K. Pecharsky, Anisotropy induced anomalies in $Dy_{1-x}Tb_x Al_2$, J. Mater. Chem. C. 5 (2017) 896–901. https://doi.org/10.1039/C6TC05384J.

[12] P.O. Ribeiro, B.P. Alho, R.S. de Oliveira, E.P. Nóbrega, V.S.R. de Sousa, P.J. von Ranke, Y. Mudryk, V.K. Pecharsky, Magnetothermal properties of $Tm_xDy_{1-x}Al_2$ (x = 0.25, 0.50 and 0.75), J.

Alloys Compd. 858 (2021) 157682. https://doi.org/10.1016/j.jallcom.2020.157682.

[13] M. Khan, K.A. Gschneidner, V.K. Pecharsky, Spin reorientation transitions in $Ho_{1-x}Dy_xAl_2$ alloys, J. Appl. Phys. 110 (2011) 103912. https://doi.org/10.1063/1.3662949.

[14] S.G. Sankar, S.K. Malik, V.U.S. Rao, Crystal field effects on the magnetocrystalline anisotropy in $HoAl_2$, J. Solid State Chem. 18 (1976) 303–306. https://doi.org/10.1016/0022-4596(76)90110-9.

[15] V.S.R. de Sousa, L.E.L. Silva, A.M. Gomes, P.J. von Ranke, Spin reorientations and crystal field modification in $Ho_{1-y}Gd_yAl_2$ compounds, J. Alloys Compd. 686 (2016) 522–525. https://doi.org/10.1016/j.jallcom.2016.06.036.

[16] Y. Mudryk, D. Paudyal, A.K. Pathak, V.K. Pecharsky, K.A. Gschneidner, Balancing structural distortions via competing 4f and itinerant interactions: a case of polymorphism in magnetocaloric $HoCo_2$, J. Mater. Chem. C. 4 (2016) 4521–4531. https://doi.org/10.1039/C6TC00867D.

[17] T. Numazawa, K. Kamiya, T. Utaki, K. Matsumoto, Magnetic refrigerator for hydrogen liquefaction, Cryogenics. 62 (2014) 185–192. https://doi.org/10.1016/j.cryogenics.2014.03.016.

[18] I. Park, S. Jeong, Development of the active magnetic regenerative refrigerator operating between 77 K and 20 K with the conduction cooled high temperature superconducting magnet, Cryogenics. 88 (2017) 106–115. https://doi.org/10.1016/j.cryogenics.2017.09.008.

[19] B.P. Alho, P.O. Ribeiro, T.S.T. Alvarenga, A.M.G. Carvalho, P.J. Von Ranke, Magnetocaloric effect in $Gd_{(1-y)}Dy_yAl_2$, Int. J. Refrig. 37 (2014) 297–302. https://doi.org/10.1016/j.ijrefrig.2013.07.012.

[20] P.O. Ribeiro, B.P. Alho, T.S.T. Alvarenga, E.P. Nóbrega, V.S.R. de Sousa, A.M.G. Carvalho, A. Caldas, N.A. de Oliveira, P.J. von Ranke, Theoretical investigations on magnetocaloric effect in $Er_{1-x}Tb_xAl_2$ series, J. Magn. Magn. Mater. 379 (2015) 112–116. https://doi.org/10.1016/j.jmmm.2014.12.023.

[21] K.R. Lea, M.J.M. Leask, W.P. Wolf, The raising of angular momentum degeneracy of f-Electron terms by cubic crystal fields, J. Phys. Chem. Solids. 23 (1962) 1381–1405. https://doi.org/10.1016/0022-3697(62)90192-0.

[22] H.G. Purwins, A. Leson, Magnetic properties of (rare earth)Al_2 intermetallic compounds, Adv. Phys. 39 (1990) 309–403. https://doi.org/10.1080/00018739000101511.

[23] N.A. de Oliveira, P.J. von Ranke, Theoretical aspects of the magnetocaloric effect, Phys. Rep. 489 (2010) 89–159. https://doi.org/10.1016/j.physrep.2009.12.006.

[24] K.W.H. Stevens, Matrix Elements and Operator Equivalents Connected with the Magnetic Properties of Rare Earth Ions, Proc. Phys. Soc. Sect. A. 65 (1952) 209–215. https://doi.org/10.1088/0370-1298/65/3/308.

[25] M.T. Hutchings, Point-Charge Calculations of Energy Levels of Magnetic Ions in Crystalline

Electric Fields, in: 1964: pp. 227–273. https://doi.org/10.1016/S0081-1947(08)60517-2.

[26] P.O. Ribeiro, B.P. Alho, T.S.T. Alvarenga, E.P. Nóbrega, A.M.G. Carvalho, V.S.R. de Sousa, A. Caldas, N.A. de Oliveira, P.J. von Ranke, Theoretical investigations on the magnetocaloric and barocaloric effects in $Tb_yGd_{(1-y)}Al_2$ series, J. Alloys Compd. 563 (2013) 242–248. https://doi.org/10.1016/j.jallcom.2013.02.068.

[27] N.W. Ashcroft, N.D. Mermin, Solid State Physics, Saunders College Publishing, 1976.

[28] G.X. Tang, W. Nolting, Magnetic properties of disordered Heisenberg binary spin system with long-range exchange, Phys. Rev. B. 73 (2006) 024415. https://doi.org/10.1103/PhysRevB.73.024415.

[29] B. Barbara, M.F. Rossignol, H.-G. Purwins, E. Walker, Magnetization Behaviour of $DyAl_2$ and $GdAl_2$, in: Cryst. F. Eff. Met. Alloy., Springer US, Boston, MA, 1977: pp. 148–152. https://doi.org/10.1007/978-1-4615-8801-6_25.

[30] K.A. Gschneidner, V.K. Pecharsky, S.K. Malik, The $(Dy_{1-x}Er_x)Al_2$ Alloys as Active Magnetic Regenerators for Magnetic Refrigeration, in: Adv. Cryog. Eng. Mater., Springer US, Boston, MA, 1996: pp. 475–483. https://doi.org/10.1007/978-1-4757-9059-7_63.

[31] B.P. Alho, A.M.G. Carvalho, P.J. von Ranke, A discussion on the magnetization calculation in polycrystalline antiferromagnetic system: Application to $EuTiO_3$, J. Magn. Magn. Mater. 324 (2012) 210–214. https://doi.org/10.1016/j.jmmm.2011.08.014.

Figure Captions

Figure 1 Temperature dependencies of the heat capacities of (a) $HoAl_2$, (b) $Ho_{0.95}Dy_{0.05}Al_2$, (c) $Ho_{0.90}Dy_{0.10}Al_2$, (d) $Ho_{0.85}Dy_{0.15}Al_2$, (e) $Ho_{0.75}Dy_{0.25}Al_2$ and (f) $Ho_{0.50}Dy_{0.50}Al_2$ measured in zero magnetic field. The symbols are the data of experimental measurements [13] and the solid lines are computed using the formalism described in Section 3.

Figure 2 Exchange parameters (λ_{HoHo}, λ_{DyDy} and λ_{HoDy}) shown as functions of Dy concentration x_{Dy}.

Figure 3 Temperature dependencies of the heat capacity in $\mu_0 H = 1$ T applied magnetic field for (a) $HoAl_2$, (b) $Ho_{0.95}Dy_{0.05}Al_2$, (c) $Ho_{0.90}Dy_{0.10}Al_2$, (d) $Ho_{0.85}Dy_{0.15}Al_2$, (e) $Ho_{0.75}Dy_{0.25}Al_2$, and (f) $Ho_{0.50}Dy_{0.50}Al_2$. Symbols represent experimental measurements and lines represent theoretical simulations. The gray lines represent simple averages $C_p^{iso}(T) = \left[C_p^{\vec{H}||<100>}(T) + C_p^{\vec{H}||<110>}(T) + C_p^{\vec{H}||<110>}(T)\right]/3$, and colored lines depict averages computed using Eq. 8.

Figure 4 Illustration of the correlation of cartesian (x, y, z) and spherical coordinates (r, θ, ϕ), for the applied magnetic field ($\mu_0\vec{H}$). In spherical coordinates, $\mu_0\vec{H}$ is described as $(r, \theta, \phi) = (\mu_0 H, \theta_i, \phi_j)$.

Figure 5 Magnetization components M_X, M_Y and M_Z of each rare-earth sublattice *vs.* temperature with $\mu_0 H = 1$ T magnetic field applied along direction with $\theta_i = 18.4\,°$ and $\phi_j = 67.3°$. Solid lines are for Ho and dashed lines are for Dy sublattices.

Figure 6 Temperature dependencies of isothermal entropy change upon magnetic field change of $\mu_0 \Delta H = 1$ T for (a) $HoAl_2$, (b) $Ho_{0.95}Dy_{0.05}Al_2$, (c) $Ho_{0.90}Dy_{0.10}Al_2$, (d) $Ho_{0.85}Dy_{0.15}Al_2$, (e) $Ho_{0.75}Dy_{0.25}Al_2$ and (f) $Ho_{0.50}Dy_{0.50}Al_2$. The symbols are the experimental measurements and the solid lines are the theoretical simulations. The gray lines represent the simple average with the magnetic field along three main crystallographic directions, and the colored lines represent averaging according to Eq. (8).

Figure 7 Temperature dependencies of adiabatic temperature change upon magnetic field change of $\mu_0 \Delta H = 1$ T for (a) $HoAl_2$, (b) $Ho_{0.95}Dy_{0.05}Al_2$, (c) $Ho_{0.90}Dy_{0.10}Al_2$, (d) $Ho_{0.85}Dy_{0.15}Al_2$, (e) $Ho_{0.75}Dy_{0.25}Al_2$ and (f) $Ho_{0.50}Dy_{0.50}Al_2$. The symbols are the experimental measurements and the solid lines are the theoretical simulations. The gray lines represent the simple average with the magnetic field along three main crystallographic directions, and the colored lines represent averaging according to Eq. (8).

Figure 8 Isothermal entropy change vs. temperature for (a) $Ho_{0.90}Dy_{0.10}Al_2$ and (b) $Ho_{0.50}Dy_{0.50}Al_2$, upon applied magnetic field change of $\mu_0 \Delta H = 2$ T. The symbols are the new experimental measurements and the solid lines the theoretical simulations calculated with an average of the main cubic directions: $\langle 100 \rangle, \langle 110 \rangle$ and $\langle 111 \rangle$.

Figure 9 Adiabatic temperature change vs. temperature for (a) $Ho_{0.90}Dy_{0.10}Al_2$ and (b) $Ho_{0.50}Dy_{0.50}Al_2$, upon applied magnetic field change of $\mu_0 \Delta H = 2$ T. The symbols are the new experimental measurements and the solid lines the theoretical simulations calculated with an average of the main cubic directions: $\langle 100 \rangle, \langle 110 \rangle$ and $\langle 111 \rangle$.